INL/MIS-21-63102-Revision-0

Modeling and Simulation of Advanced Manufacturing Techniques using MOOSE and MALAMUTE

November 2023

Stephanie A Pitts, Sudipta Biswas, Dewen Yushu, Alexander D Lindsay, Wen Jiang, Larry K Aagesen Jr

Changing the World's Energy Future

INL is a U.S. Department of Energy National Laboratory operated by Battelle Energy Alliance, LLC

INL/MIS-21-63102-Revision-0

Modeling and Simulation of Advanced Manufacturing Techniques using MOOSE and MALAMUTE

Stephanie A Pitts, Sudipta Biswas, Dewen Yushu, Alexander D Lindsay, Wen Jiang, Larry K Aagesen Jr

November 2023

Idaho National Laboratory
Idaho Falls, Idaho 83415

http://www.inl.gov

Prepared for the
U.S. Department of Energy
Under DOE Idaho Operations Office
Contract DE-AC07-05ID14517, DE-AC07-05ID14517, DE-AC07-05ID14517, DE-AC07-05ID14517

Chapter 13: Modelling and Simulation of Advanced Manufacturing Techniques using MOOSE and MALAMUTE

Authors: Stephanie A. Pitts, Sudipta Biswas, Dewen Yushu, Alexander D. Lindsay, Wen Jiang, Larry K. Aagesen (Idaho National Laboratory)

1.1.1 Abstract

Advanced manufacturing techniques offer increased geometry complexity, energy and material usage efficiency improvements, and an expanded palette of materials as compared to conventional manufacturing approaches. Advanced-manufacturing-produced parts can experience wide variations in the final microstructure, and these microstructure variations significantly impact the parts' performance. In this chapter, we present recent code developments within Multiphysics Object-Oriented Simulation Environment (MOOSE) and in the MOOSE Application Library for Advanced Manufacturing UTilitiEs (MALAMUTE). Here we demonstrate applying these modeling and simulation codes to two advanced manufacturing process types: advanced sintering techniques and laser-based additive manufacturing techniques. The multiphysics and multiscale capabilities of these codes enable prediction of the microstructure evolution resulting from variations in the Advanced manufacturing process parameters.

1.1.2 Introduction

Advanced manufacturing (AM), an umbrella term encompassing many different technologies, enables the production of complex parts not readily accessible through traditional manufacturing approaches. AM techniques are characterized as innovative processes promising energy efficiency and rapid production (United States Department of Energy, Office of Energy Efficiency and Renewable Energy, 2019) (Manière, Lee, McKittrick, & Olevsky, 2018). While achieving these goals, the requirement for improved and reliable material performance is paramount for materials in extreme environment applications, including the nuclear industry.

AM techniques use advanced materials, such as refractory metals and high-entropy alloys, that can withstand the ultra-high temperatures and radiation conditions anticipated in some nuclear reactor designs but are difficult to manufacture through conventional processes (Xia, Gao, Yang, Liaw, & Zhang, 2016) (Kareer, et al., 2019). Often another advantage of AM techniques is producing near-net-shape geometries; the near-net-shape production enables more efficient use of the source material (Li, Post, Kunc, Elliott, & Paranthaman, 2017) (Gibson, Rosen, & Stucker, 2015). Near-net-shape manufacturing produces capabilities enable the production of complex geometries not readily feasible with traditional approaches. The interior cavities that additive manufacturing techniques can produce remain a classic example of a geometrical feature unattainable with traditional subtractive manufacturing.

The microstructural features of materials produced by AM techniques are significantly different from conventionally manufactured materials (Smith, et al., 2016). Small changes in even a few manufacturing process parameters can have significant effects on the resulting microstructure. Due to such variations in microstructure, qualifying AM products for various extreme environment applications is challenging. Modeling and simulation provide a cost-effective way to establish and evaluate the process-structure-property-performance (PSPP) correlation for the AM products by regulating the manufacturing process parameters. Establishing PSPP correlations for AM techniques can be achieved through developing multiscale, physics-informed models. These computational models can be used to refine manufacturing processes based on the potential application.

In this chapter, we will discuss AM research and development efforts complete with the Multiscale Object-Oriented Simulation Environment (MOOSE) and derived applications. MOOSE is a multiphysics, multiscale simulation tool developed at Idaho National Laboratory (INL) in an open-source manner to encourage and facilitate interdisciplinary collaboration (Permann, et al., 2020). Established physics, such as solid and fluid mechanics, fluid-structure interaction, electromagnetics, thermo-mechanical contact, and microstructural evolution, are packaged in MOOSE modules. The MOOSE Application Library for AM UTilitiEs (MALAMUTE) combines the physics from MOOSE modules with advanced material models and geometries to model AM processes. Here we will also present a set of simulation approaches, implemented through MALAMUTE, for two AM methods, advanced sintering techniques and laser-based additive manufacturing techniques, as applied to ceramics and metals. Advanced sintering techniques, such as the electric field assisted sintering (EFAS) technique, are employed to manufacture advanced porous fuel and integrated fuel-cladding material for new reactor designs. Laser-based additive manufacturing techniques, including directed energy deposition (DED) and laser powder bed fusion techniques, are gaining popularity because of their ability to produce near-net-shape, complex structures with desirable mechanical properties and reduced material waste in a compressed timeframe.

1.1.3 Advanced Sintering Techniques

Sintering, a prevalent material processing technique in powder metallurgy, compacts powder particles into a solid polycrystalline structure with reduced surface area and increased density. Several materials with high-melting points and that are difficult to process with conventional approaches can easily be manufactured with sintering. Conventional solid-state sintering methods focus on coalescing powder particles by applying heat and pressure, without melting the material. Densification, in this case, is activated due to mass diffusion, plastic flow, or both. The EFAS technique is a powder metallurgy technique developed from sintering. As in conventional sintering, the metal or ceramic powder to be formed into the part is placed within a graphite die, and the die is placed between two rams.

The EFAS's hallmark is applying an electrical current, often pulsed direct current. This current is combined with a uniaxial pressure to sinter the powders within a vacuum or inert environment, as shown in Figure 1. EFAS is also commonly known as spark plasma sintering (SPS) from an early hypothesis that a plasma forms during the manufacturing process between the powder particles; however, no experimental evidence of a plasma forming has been measured, and recent calculations suggest the formation of a plasma is unlikely (Anselmi-Tamburini, et al., 2012). Still the misnomer remains commonly used. EFAS is gaining industry recognition and adoption because of its significantly shorter processing time and lower processing pressures compared to conventional approaches [7].

Electrical resistivity within the graphite die, and in some cases within the powder as well, produces a rapid increase in temperature due to Joule heating as the electrical current is passed through the assembly, producing a fine-grain microstructure (Anselmi-Tamburini & Groza, 2017). Retaining fine, or small, grains in the final part microstructure is a significant advantage of EFAS manufacturing: other powder metallurgy techniques, such as hot pressing, produce large-grained microstructures. The capability to produce a fine-grained microstructure is critical because control over the final microstructure characteristics improves engineering-scale material performance.

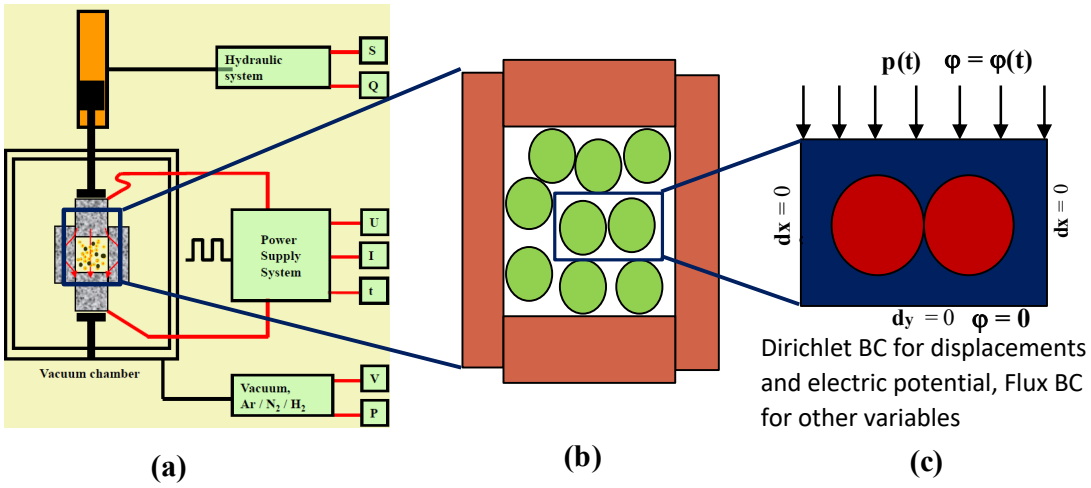

Figure 1. Schematic of the modeling simplifications: Overview of the EFAS manufacturing process (a); Idealization of the sintering die (b); Simplified geometry adopted in the mesoscale modeling (c). (Figure reproduced from (Biswas, Schwen, Singh, & Tomar, 2016))

Electric field assisted sintering and related sintering techniques have only a few manufacturing process parameters: current, pressure, and temperature. Modeling and simulation tools are being developed to predict how variations in these three process parameters influence the final part microstructure. These predictions will help determine how to apply these process parameters to produce the desired final microstructure consistently and reliably. At INL, we are developing a high-fidelity modeling and simulation capability to examine how process parameters determine the microstructure evolution through the EFAS manufacturing technique, focusing on the manufacturing technique from the green-body compact to the end of the temperature hold period. This development work has been conducted on the metal silver and the ceramic yttrium oxide within MOOSE and MALAMUTE.

1.1.3.1 Microstructural Evolution

Understanding the densification mechanisms and microstructural evolution during the sintering process is important to correlate the process parameters to the final product. This understanding provides a key connection for establishing the PSPP correlation for sintering. Here, a phase-field modeling (PFM) approach is employed to demonstrate the morphological transformations during the sintering process. PFM is a diffuse interface approach that captures the microstructural evolution by the minimizing the excess thermodynamic energy of the system (Moelans, Blanpain, & Wollants, 2008; Steinbach, 2009). As described in Figure 1, the microstructural model is simplified to two particles for closely monitoring the densification mechanisms.

At the microstructural level, the consolidation happens in three stages due to a combination of mass diffusion mechanisms (see Figure 2a). In Stage I, a neck between two particles is formed and the shape of the individual particles change; in Stage II, a stabilized neck length is achieved, and the grain coarsening initiates; finally, in Stage III, the coarsening continues where one particle grows at the expense of the other particle (Biswas, Schwen, & Tomar, Implementation of a phase field model for simulating evolution of two powder particles representing microstructural changes during sintering, 2018). The transition between different stages depends on the material properties and the sintering conditions. Figure 2b illustrates the neck formation between two silver nanoparticles during pressure-less sintering; the rate of neck growth is higher during Stage I and reduces as the neck length stabilizes at Stage II. No grain coarsening is observed in this case. Figure 2b also demonstrates the accuracy of 2D vs. 3D simulations as compared to experimental observations

(Asoro, Ferreira, & Kovar, 2014; Biswas, Multiphysics modeling for predicting microstructural evolution of powder materials during solid-state sintering, 2017). Compared to the experimental data and the 3D simulations, the 2D simulations underpredict the rate of densification.

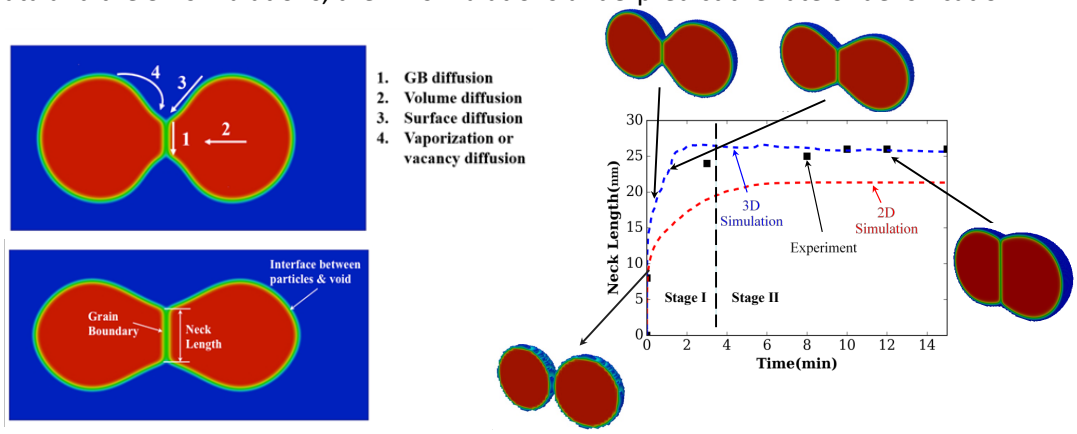

(a) (b)

Figure 2. Interface evolution during sintering along with the contributing mechanisms (red indicates the solid particles, blue region is the void area surrounding the particles, and green is the diffuse interface between the two) (Biswas, Schwen, Singh, & Tomar, 2016; Verma, Biswas, Prakash, & Tomar, 2017)(a); Neck formation and growth during sintering of two silver nanoparticles (b) (Figure reproduced from (Biswas, Multiphysics modeling for predicting microstructural evolution of powder materials during solid-state sintering, 2017)).

We leverage the multiphysics coupling capabilities of MOOSE to couple a thermal analysis with the phase-field model described above. The effect of temperature, especially of heating during the sintering process, can be incorporated through this coupling. However, at the mesoscale, the simulation domain is not large enough for a heat source on the boundary to induce thermal gradient across the domain, and uniform temperature distribution across the simulation domain is achieved within few time steps. Hence, uniform temperature assumption can be made for these simulations (Biswas, Schwen, & Tomar, Implementation of a phase field model for simulating evolution of two powder particles representing microstructural changes during sintering, 2018).

To explore the role of mechanical loading on the particle morphology during pressure-assisted sintering techniques, an elastic energy contribution is added to the PFM (Biswas, Schwen, Singh, & Tomar, 2016; Biswas, Schwen, & Tomar, Implementation of a phase field model for simulating evolution of two powder particles representing microstructural changes during sintering, 2018). With an increase in mechanical loading, the amount of material undergoing deformation and associated strain energy of the system rises. This increasing strain energy contributes to the system's total free energy and to the driving force for the densification. Applying an external load also reduces the volume available for the powder, further facilitating the densification. Figure 3 demonstrates the temporal evolution of multiple particles under pressure-assisted sintering. At the initial stage (see Figure 3a), the particles are only in contact with each other. Over time, the individual particles transform into a polycrystalline material with reduced porosity. The particle compaction, in this case, is primarily governed by the surface and grain boundary diffusion. We note particles on the edges consolidate faster than the intermediate ones (see Figure 3). At later stages, coarsening initiation is visible (see Figure 3e and Figure 3f). The final density of the compacted structure increases with the maximum applied pressure.

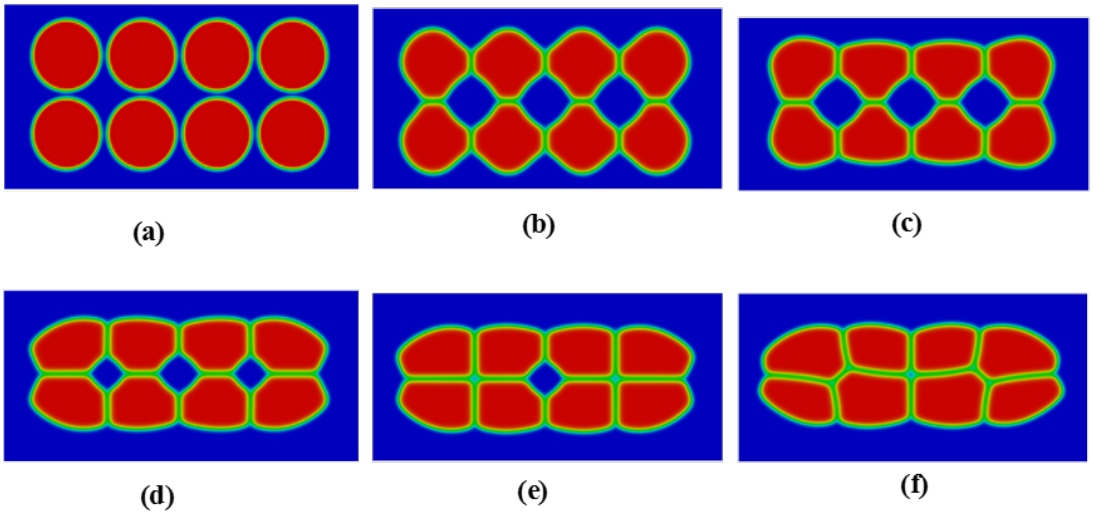

Figure 3. Microstructural evolution of multi-particles during pressure-assisted sintering process (Biswas, Schwen, Singh, & Tomar, 2016).

Mesoscale modeling of sintering techniques is an ongoing area of research, and here we have provided only a brief overview of the mechanisms responsible for densification at the microstructural level. For advanced sintering techniques, the inclusion of additional physics, beyond those discussed above, may be necessary. Different PFMs are available for handling complex material systems (Greenquist, Tonks, Aagesen, & Zhang, 2020; Biswas, Schwen, Wang, Okuniewski, & Tomar, 2018). For high-pressure sintering, plastic flow and large deformation must be considered (Averú, Biehl, Medeiros, & Souza, 2016). Developing these additional phase-field model terms will improve the microstructure predictions.

1.1.3.2 Engineering-Scale Process Model

The electric potential, temperature, and stress and strain distribution through the EFAS rams and tooling dictate the conditions to which the mesoscale powder particles are subjected. Connecting the influence of the process parameters to the final part microstructure has been explored through several engineering-scale simulations (Cincotti, Locci, Orrù, & Cao, 2007). Leveraging the multiphysics capabilities of MOOSE and MALAMUTE, we have performed electro-thermo-mechanical simulations of the EFAS engineering-scale system. The material properties of both the EFAS assembly components and yttrium oxide are allowed to evolve with temperature. Electrical and thermal contact between all dissimilar materials in the assembly is modeled with a harmonic mean approach (Cincotti, Locci, Orrù, & Cao, 2007). Mechanical contact is included only between the die tooling and yttrium oxide geometry components; only these components are expected to experience significant deformation at the engineering scale.

Figure 4 shows the resulting electric potential, temperature, and effective von Mises stress fields across a standalone graphite tooling and powder geometry. An electric potential difference of 0.8 V, ramped from 0 V over a 20-second period and then held constant, is applied to the top of the upper plunger stem. Zero displacement boundary conditions are applied to the top and bottom of the upper and lower plunger stems, respectively. The simulation is run for a total of 7 minutes to investigate the system response during the EFAS process initial stages. The electric potential is modeled with Maxwell's equations (Icenhour, Lindsay, Martineau, & Shannon, 2019). Heat conduction and thermal radiation are considered in the thermodynamics analysis, and the materials are treated as isotropic elastic in the solid mechanics calculation. Thermal expansion in the graphite tooling increases as the non-uniform temperature rise. Since this simulation is performed without

the graphite spacers and rams of the EFAS system, the temperatures shown in Figure 4 are significantly lower than those experimentally measured.

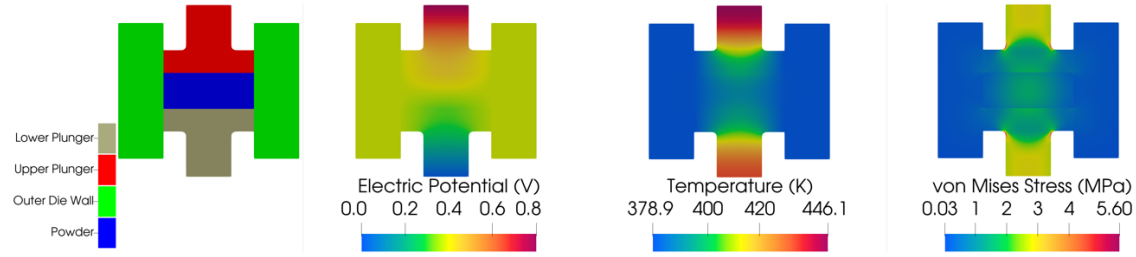

Figure 4. Cross-section of a multiphysics simulation of the EFAS graphite tooling (stepped plungers and outer die wall) and the yttrium oxide powder in an engineering-scale model using MALAMUTE (a). An applied electric potential difference (b) produces a temperature increase through Joule heating (c). Mechanical stress develops from the thermal expansion eigenstrain (d).

While there is general adoption of similar approaches to modeling the rams and graphite tooling, modeling the powder remains an area of active research (Locci, Orrù, & Cao, 2020). The EFAS manufacturing process is inherently multiscale, as evident from Figure 1. While the electrical current and pressure are applied to the entire manufacturing system on the length scale of meters and millimeters, the powder particle coalescence and densification occur on the length scale of micrometers and nanometers. The engineering-scale electro-thermo-mechanical behavior is linked intricately to the microstructure of the sintered part. Modeling the influence of the EFAS process parameters on the final part microstructure requires a simulation approach encompassing all these length scales.

1.1.3.3 Multiscale Modeling Approach

Utilizing the multiscale capabilities within MOOSE, we transfer the data from the high-fidelity lower length scale simulations to the homogeneous engineering-scale simulation in two stages (see Figure 5). This approach enables the use of a more computationally efficient homogeneous simulation of the powder. The relevant microstructure physics are captured in high-fidelity, computationally intensive, lower length scale simulations while the homogeneous powder model is used within the engineering-scale model of the complete EFAS system.

Particle-particle contact simulations are run with a series of different particle arrangements. These mesoscale mechanical contact simulations are used to construct a power-law creep-type constitutive reduced-order model, following (Casagranda & Sofronis, 1997). This constitutive model is used in the engineering-scale simulation to describe the powder's mechanical response, particularly at the lower densification regimes early in the manufacturing process.

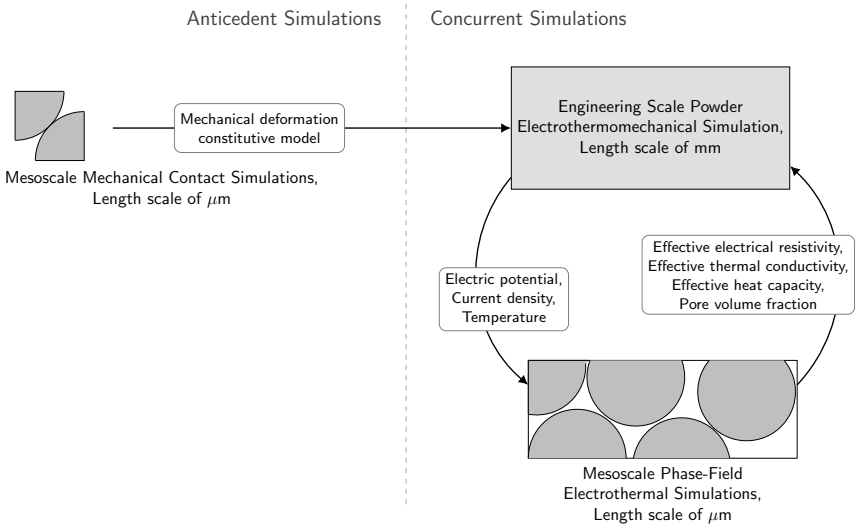

Figure 5: Schematic of the multiscale approach used to model the EFAS technique, with both separate antecedent and concurrent mesoscale simulations; the latter employs the MOOSE MultiApp capability to run different mesoscale simulations at multiple individual locations throughout the engineering-scale domain.

Engineering-scale simulations of the powder act as the framework for the electro-thermal coupling, shown on the right of Figure 5. Through the MOOSE MultiApp system (Gaston, et al., 2015), several mesoscale PFM simulations are run at different locations throughout the engineering-scale domain. Local conditions at each point in the engineering-scale domain are applied as boundary or input conditions to each individual mesoscale simulation. The electrical potential value and the current density are applied to the top and bottom boundaries of the PFM simulation mesh, respectively, and the temperature is applied as a uniform field. These PFM simulations perform the electro-thermal analysis described above and track the evolution of the particle morphologies. The effective electrical and thermal properties are calculated and passed back to the engineering-scale domain.

Continuing and future developments for modeling the EFAS technique will include expanding the multiscale data coupling through the MultiApp system with a particular focus on incorporating concurrent mechanical simulations. Future efforts to expand the mesoscale models to include additional physics-based terms to capture local charge build-up and dissipation of particle coatings should be explored. On the engineering scale, a robust treatment of the heat loss from the graphite tooling is recommended as another area for future development efforts. Verification of these models is ongoing, and validation efforts are needed for the coupled multiscale models.

1.1.4 Laser-Based Additive Manufacturing Processes

Additive manufacturing, or 3D printing, refers to the processes of fabricating objects layer-by-layer directly from computer-generated geometry models. Additive manufacturing processes can be classified into several categories, such as directed energy deposition (DED) (ASTM Committee F42 on Additive Manufacturing Technologies and ASTM Committee F42 on Additive Manufacturing Technologies. Subcommittee F42. 91 on Terminology, 2012) and powder bed fusion techniques. A wide variety of materials, such as ceramic, glass, metals, polymers, and composite materials, can be fabricated by additive manufacturing techniques (Sun, et al., 2021). Additive manufacturing techniques are being invested for use in new nuclear reactor applications requiring complex geometry parts, such as microreactors (Sridharan, Gussev, & Field, 2019), and applications involving difficult-to-assemble components, such as the ITER first wall assembly (Zhong, et al., 2017).

During a laser-based additive manufacturing process, a high-intensity moving energy source strikes the metal powders. This energy source melts the material, allowing the material to be deposited on a substrate, as in DED and 3D printing techniques, or to form a local melt pool, as in powder bed fusion techniques. The heat will transfer by convection and conduction and create a non-uniform temperature profile. The resulting non-uniform temperature profile and residual stresses will significantly impact the resulting final part microstructure. As with the advanced sintering techniques, laser-based additive manufacturing techniques can be easily characterized as nonlinear and non-equilibrium processes requiring a multiphysics modeling approach. Engineering-scale and mesoscale high-fidelity physics-based numerical models are being developed at INL to evaluate laser-based additively manufactured part microstructure and to provide insight for process improvements. These modeling approaches also employ the MultiApp and multiphysics capabilities within MOOSE.

In this section, we will discuss three different capabilities being developed within MOOSE and MALAMUTE for laser-based manufacturing applications. A novel element activation, or element birth, method is being developed for modeling material deposition. To model the process of melt-pool formation and to track the moving interface between the liquid metal and air, both level-set method and arbitrary Lagrangian-Eulerian (ALE) approaches have been developed. In each approach, the effect of the focused thermal energy is modeled by a moving heat source associated with the laser scanning path. Although we show only a few examples here, the methods and capabilities introduced in this section are generally applicable and extendable to other types of additive manufacturing techniques.

1.1.4.1 Element Activation Capability

As one of the widely used additive manufacturing techniques, DED forms 3D products by melting material as it is being deposited on the substrate. DED is capable of fabricating with multiple materials, enabling the production of parts with functionally graded materials. The DED process allows for the production and repair of parts and has been used throughout the entire product lifecycle for applications ranging from materials research to functional prototyping to volume manufacturing (Dass & Moridi, 2019). The major disadvantages of DED includes rough finishing surface, high equipment cost, and residual stress.

Based on MOOSE's block restrictable interface (Permann, et al., 2020), which supports computations being performed on a subset of the physical domain, a novel element activation approach, developed at INL, is used to model the deposition of material during a DED process. We developed a moving subdomain paradigm to realize material addition. The physical domain is divided into an active subdomain and an inactive subdomain. The active subdomain includes the part of the product being built, along with the substrate, while the inactive subdomain is comprised of the product component yet to be built. As material is deposited during the DED process, elements are moved from the inactive subdomain to the active subdomain, expanding the active subdomain and shrinking the inactive subdomain correspondingly. An example demonstrating material deposition modeling and active/inactive subdomains is included in Figure 6.

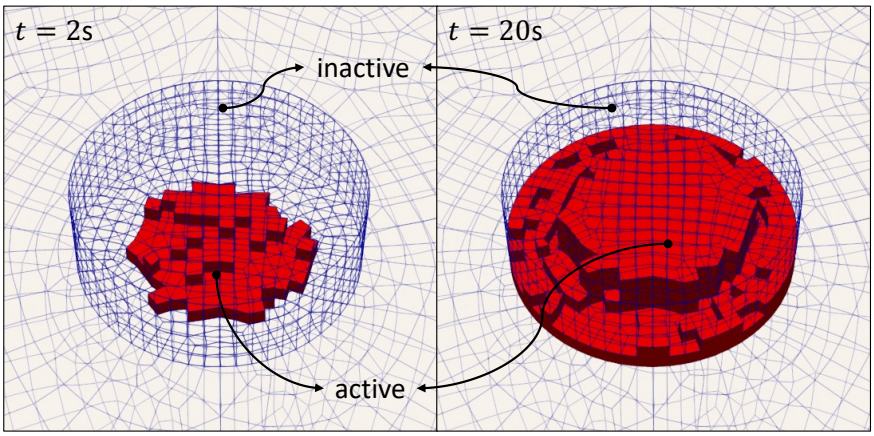

Figure 6. An example of the active and inactive subdomains of a cylinder product on the substrate at two different timesteps. The active subdomain of the product is shown in red. The inactive subdomain is shown as blue wireframe. The active subdomain expands during material deposition.

The nomenclature of active/inactive subdomains is used here to indicate the region in which the coupled thermo-mechanical finite element computation is performed. The inactive subdomain contains only geometric information. This approach greatly improves the efficiency of the overall computation compared to other approaches (e.g., (Stender, et al., 2018)) that perform the computation across the entire physical domain at every timestep.

There are currently two element activation modes in MOOSE: activation by path and activation by temperature. The former approach activates the elements close to the laser beam scanning path. An activation distance is set to control the amount of material been deposited. Using this approach, both the mechanical and thermal analyses are performed only in the active subdomain. In contrast, the latter approach activates those elements having an average temperature below a user-defined threshold value. To mimic the material solidification process, the threshold temperature is often set to be the material's melt temperature.

To model the moving heat source produced by the scanning laser beam, we employ a Gaussian point heat source; this method is widely used for laser heat-source modeling (Hussein, Hao, Yan, & Everson, 2013). To mimic the motion of the heat source, we consider the heat source's center to coincide with the scanning path. Here we model the scanning path as a moving point in 3D space varying with the product geometry and the manufacturing process design. We consider an effective radius of the laser beam such that material points that are far-away (2x effective radius) from the center of the laser beam are subject to a total of 5% of the laser power. A larger effective radius will reduce the peak value of the heat source. Figure 7 shows examples of the heat source with varying effective radii.

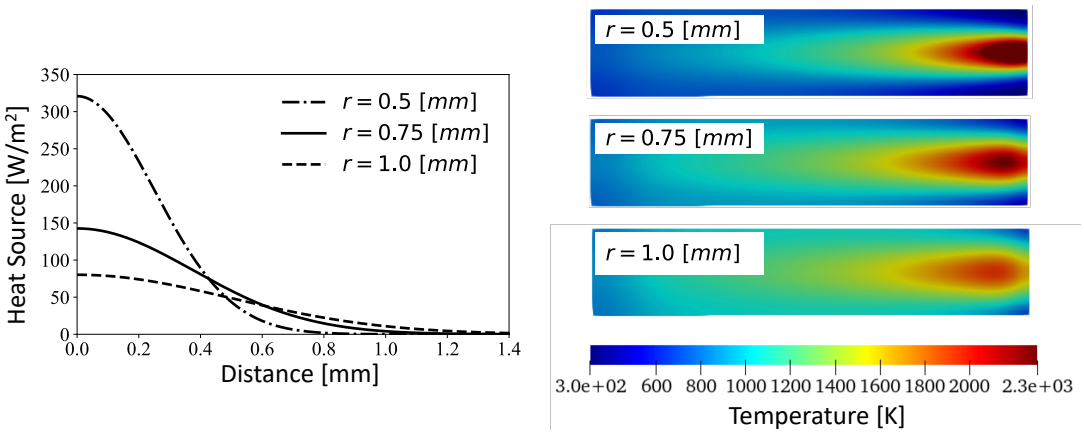

(a) (b)

Figure 7. Heat source with different effective radii (*r*). Heat-source value as a function of distance from the center (a). The temperature fields of a rectangular plate under horizontal laser scans (b).

To accurately predict the distortion, residual stress, and mechanical properties of the DED-manufactured product, we employ a thermo-mechanical model. The thermal model includes the heat conduction equation with the moving heat source, a fixed temperature at the bottom of the substrate, and convective boundary conditions along the rest of the surfaces. The mechanical model includes the quasi-static conservation of momentum equation with fixed zero displacement at the bottom of the substrate. The mechanical behavior of the material is described by a temperature and rate dependent constitutive relation (Stender, et al., 2018). The temperature dependence of the solid mechanics solution is modeled through two aspects: the thermally induced expansion and the temperature dependent material properties in the constitutive model.

1.1.4.2 MultiApp Modeling Design

The temperature field is obtained by solving a separate heat conduction problem in both the active/inactive subdomains while the thermo-mechanical analysis is performed only in the active subdomain. These analyses are embedded in a MultiApp. The main app solves the heat conduction problem in the entire domain, and a sub-app solves the coupled thermo-mechanical problem in the active subdomain.

As an illustration, we demonstrate the simulated printing process of an INL logo. The three letters have a total length, width, and height of 42.5 mm, 20 mm, and 10 mm, respectively. The letters lay on the substrate which has the dimension of 100 × 100 × 5 mm^3. The material constitutive model and properties are from (Stender, et al., 2018). The geometry, mesh, and rectilinear printing path are shown in Figure 8(a) and Figure 8(b). The elements are activated by the scanning path with activation distance of 1.4 mm. The laser power is set to 360W and has an effective radius of 4 mm. We present the evolution of the temperature and the von Mises stress at different timesteps in Figure 8(c) and Figure 8(d), respectively. The heating spot moves along with the laser beam, and the elements are constantly deposited around it. The product undergoes high-residual stress away from the heating spot because of the structural characteristic as well as the deposited material's rapid cooldown.

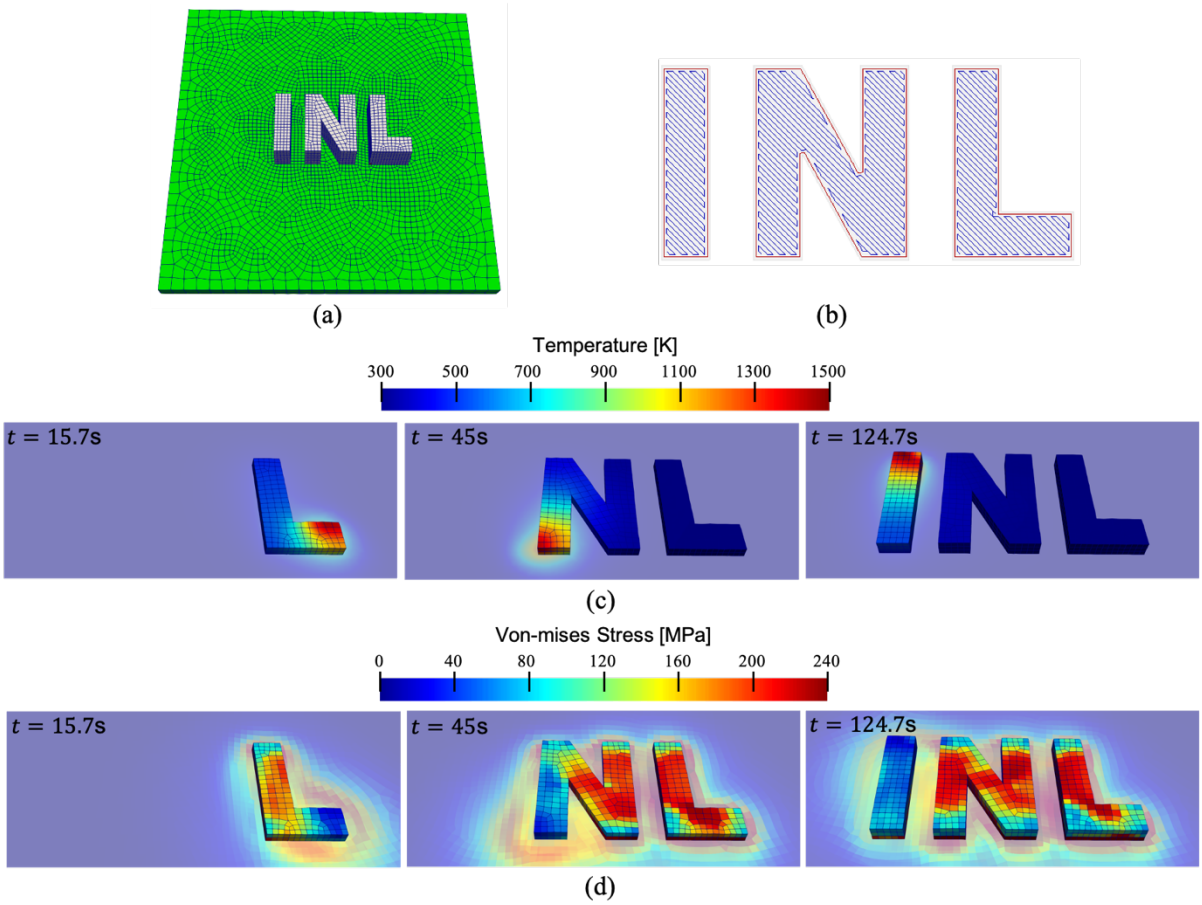

Figure 8. Thermo-mechanical printing process simulation of the INL logo: (a) Design and finite element mesh of the product and the substrate. (b) One layer of the rectilinear printing path. (c) Temperature and (d) von Mises stress fields at different timesteps.

Continuing developments are necessary to enable the use of these models for manufacturing process optimization. Verification and validation are needed for the material addition, moving heat-source modeling, material and process parameters, and thermal and mechanical constitutive equations. Second, improved multiscale simulation capabilities will allow further investigation by incorporating the predictions for particle material, melt-pool fluid flow (see later section), and the gas-liquid-solid interactions. Finally, the computational cost for these high-fidelity models remains high, preventing the direct application of the simulation model for online process optimization. Emphasis should be given to smart approaches that reduce the modeling complexity without sacrificing accuracy.

1.1.4.3 Level Set Method

During melt-pool type additive manufacturing process, a local melt pool is formed with a high-intensity moving energy source, such as a laser. A continuum finite element model can be used to describe relevant multiphysics phenomena, including the generating the powder layer, melting and solidification, melt-pool dynamics, and thermal-capillary, buoyant, conductive, and convective heat transport processes.

The level set method is an approach used to track the moving interface in melt-pool modeling. In this approach, the moving interface's location is implicitly represented by an iso-contour of the level set variable. The mesh is fixed in time, and the material moves through the mesh making this technique suitable for complex geometric changes of the interface such as the porosity's formation.

The conservative level set function (Olsson & Kreiss, 2005) is a smeared Heaviside function that goes smoothly from zero (air) to one (liquid). The interface is defined by the 0.5 iso-contour of the level set function, and it is advected by the fluid velocity and powder addition speed. The boundary conditions at the liquid-air interface are enforced by source terms that are restricted by a diffuse Dirac delta function defined by the level set variable.

In addition, the interface curvature and normal vector to the interface can be formulated by the level set variable, and these values are often required to calculate the surface tension and Marangoni forces (Wen & C.Shin, 2010) in the fluid momentum balance equation. With the level set method, the coupled highly nonlinear system typically consists of level set evolution and fluid-mass, momentum, and energy equations. With MOOSE's automatic differentiation capability (Lindsay, et al., 2021), perfect Jacobians can be formed allowing these equations to be solved in a fully coupled manner with remarkable efficiency.

We first demonstrate a DED deposition process for 316L stainless steel. The simulation details can be found in (Lindsay, et al., 2021). The predicted deposition profile and fluid motion at 0.4 seconds are shown in Figure 9. Two vortices can be seen in the melt pool, which are mainly formed by thermal-capillary forces.

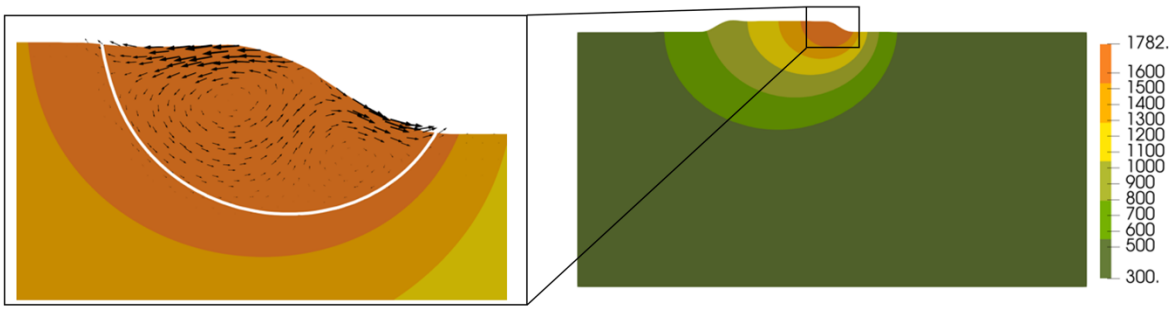

Figure 9. DED deposition profile at t = 0.4 seconds. Temperature contours range from 300 K to 1782 K. The zoomed view of the fluid motion velocity field is shown on the left, where arrows represent scaled velocity vectors, and the white line shows the contour of the melting temperature. (Figure reproduced from (Lindsay, et al., 2021))

Figure 10 shows two simple examples highlighting the advantage of the level set method on handling severe interface deformations and topology changes. On the left, keyhole formation due to strong recoil pressure (Courtois, 2014) during laser welding is demonstrated; on the right, the level set variable was initialized to represent multiple discrete powder particles. Particle melting was simulated by the melt-pool dynamics where complex melt droplets can be captured.

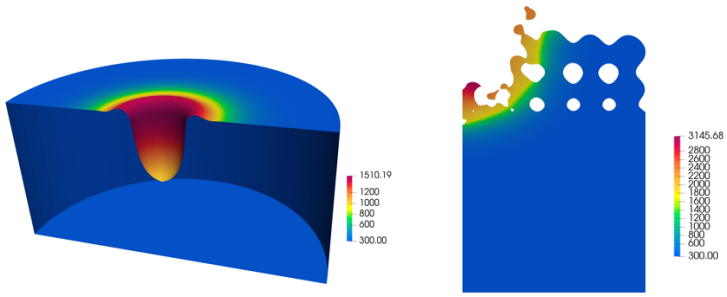

(a) (b)

Figure 10. Keyhole formation during laser welding (a); melting of multiple powder particles (b). The coloring is based on the temperature (K) contours.

Future work on the level set method will involve supporting discontinuous fields across the interface. The current continuous pressure field from the level set method produces an artificial mass transfer across the interface. To overcome this issue, the MOOSE's eXtended Finite Element Method (XFEM) capability (Jiang, Spencer, & Dolbow, 2020) can be utilized to introduce the pressure discontinuity and therefore preserve the mass. We may also develop a capability to couple level set melt- pool models and discrete particle motions to accurately capture the interaction between melt and particles. Lastly, uncertainty qualification methods can be employed to quantify the input and output uncertainties in the level set melt-pool models (Xie, Jiang, Congjian, & Xu, 2021).

1.1.4.4 Arbitrary Lagrangian-Eulerian Capability

In (Lindsay, et al., 2021) we demonstrated melt-pool evolution via the arbitrary Lagrangian-Eulerian (ALE) approach in MOOSE. The equations, boundary conditions, and material properties are based on (Noble, 2007). Pressure and velocity are determined by the transient incompressible Navier-Stokes equations, and temperature is modeled with a transient conduction-convection equation. An incident laser energy flux heats the surface and eventually begins to evaporate material, exerting a recoil force and displacing the melt pool. Additional forces are exerted by the Marangoni effect; however, these were not included in (Lindsay, et al., 2021) since remeshing is required to properly resolve tangential gradients which can lead to element inversion at the surface.

By changing the finite element Jacobian matrix, which maps the element from the reference to physical space, mesh displacement enters the residual calculation process in subtle but very important ways. Mesh displacement also changes shape function gradients, consequently modifying both local element solution gradients and test function gradients. Tracking this dependence on displacements by hand would be nearly impossible. Alternatively, a modeler may choose to use a matrix-free approximation to the Jacobian, but this approximation is subject to errors from floating-point round off that can become significant in these multiphysics problems. The melt-pool simulation conducted in (Lindsay, et al., 2021) and reproduced here includes a viscosity that varies by eight orders of magnitude. Other material properties only add to scaling complexity. For this problem matrix-free solution of melt-pool physics in MOOSE fails to converge because of the difficult scaling. However, through MOOSE's automatic differentiation system, we can form perfect Jacobians for the melt pool, enabling the results shown here.

Figure 11 shows MOOSE 3D simulation results for the ALE equations. The simulation was performed with adaptive mesh refinement based on gradient jumps in the temperature and z-displacement variables. The laser is rotated counterclockwise around the top surface of a 3D cube. When the surface reaches the boiling point of the medium, it recoils creating an imprint in the surface that tracks with the rotating laser spot. Figure 12 shows a representative 2D simulation, where the laser is swept back and forth repeatedly across the surface. As with the 3D simulation, melted material is displaced away from the impinging laser spot.

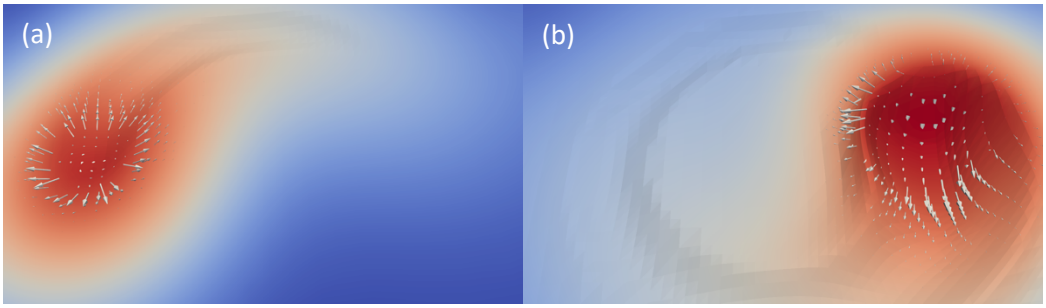

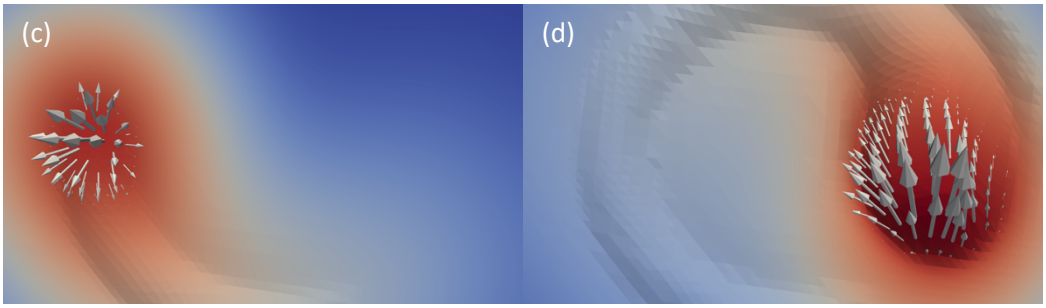

Figure 11: Visualization of the top surface of the melt pool. (a) corresponds to a half laser rotation, and (b) corresponds to a full rotation, both viewed from above. Bottom sub-figures also correspond to half (c) and full rotations (d), respectively but viewed from below. Solid coloring is based on the temperature. Arrows are based on the velocity. (Figure reproduced from (Lindsay, et al., 2021))

1.1.4.5 Microstructure Evolution and Multiscale Approach

In processes such as laser welding where a melt pool is formed on the surface of two parts being joined, local changes in the material's microstructure can result in significant changes in the properties of the material near the weld. As the melt pool resolidifies, the solidification process controls the microstructure and properties of this region. However, the heat input from the laser also causes temperatures to increase significantly outside the melt pool. The region outside the melt pool where temperatures increase enough to cause microstructural changes, but not enough to cause melting, is referred to as the heat-affected zone (HAZ) (Porter & Easterling, 1992). One of the most significant microstructural changes that can occur in the HAZ is grain growth (Porter & Easterling, 1992). Grain growth is the process by which the average size of grains increases and is a strong function of temperature. As with the EFAS modeling, it is critical to be able to predict microstructure evolution because the resulting grain structure can significantly impact the part performance.

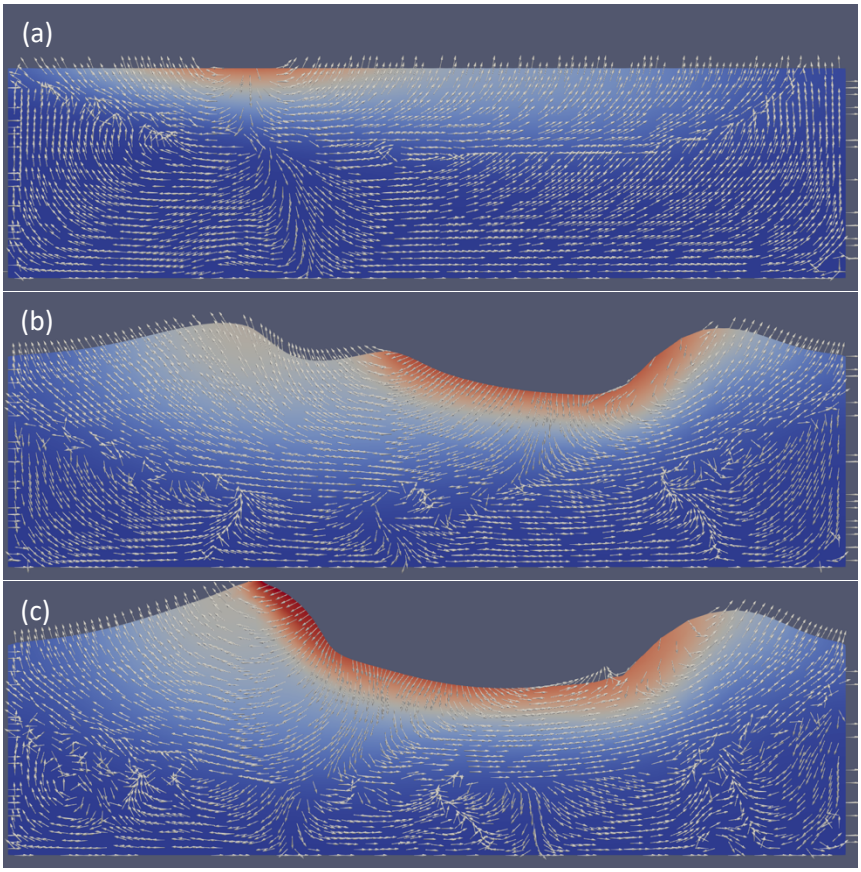

Figure 12: Two-dimensional melt-pool simulation. Arrows represent unscaled velocity vectors. Solid coloring is based on the temperature. Times in arbitrary units are (a)100, (b)200, and (c)220. (Figure reproduced from (Lindsay, et al., 2021))

To predict the final microstructure of a part processed using laser-based techniques, both the HAZ and the resolidifying melt pool should be considered. The average grain size in materials is typically much smaller than the size of engineering-scale parts, and it is not computationally practical to perform simulations of microstructural evolution of the entire component. In (Lindsay, et al., 2021) we employed the multiscale capabilities of the MOOSE framework to address this challenge.

The multiscale coupling strategy (employed in (Lindsay, et al., 2021)) uses the ALE-based model of laser melt-pool dynamics briefly described above at the engineering scale, including the temperature field in both the melt pool and the surrounding HAZ. To simulate grain growth in the HAZ, multiple instantiations of the MOOSE grain growth PFM (Moelans, Blanpain, & Wollants, 2008; Permann, Tonks, Fromm, & Gaston, 2016) are run concurrently with the engineering-scale model using the MOOSE MultiApp system (Permann, et al., 2020). Each instantiation represents microstructural evolution at a different position within the HAZ of the engineering-scale simulation domain; thus, each grain growth simulation is a representative volume element (RVE) of the macroscale simulation domain. The temperatures at each RVE's position are passed from the engineering-scale model to the corresponding grain growth simulation using the MOOSE Transfer system (Permann, et al., 2020). Figure 13 shows a schematic of the coupled simulations.

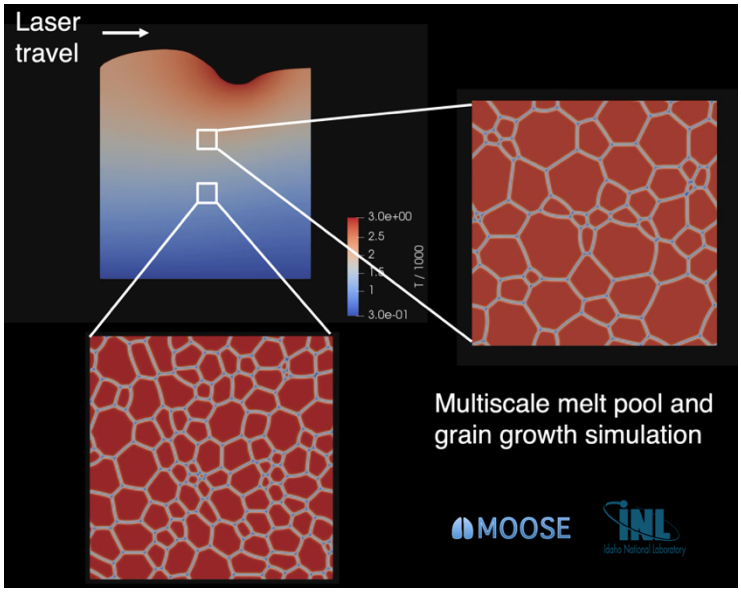

Figure 13: Multiscale demonstration of laser welding with coupled phase-field simulations to determine microstructural evolution in the HAZ. The higher temperatures for the grain growth simulations conducted nearer the surface of the macroscopic laser welding simulation result in a larger grain size. (Figure reproduced from (Lindsay, et al., 2021))

Grain growth simulations were conducted in RVEs as shown in Figure 13. The RVEs are 2D with a size of 100 × 100 μm^2. The grain structure in the initial conditions is constructed with a Voronoi tessellation as described in (Permann, Tonks, Fromm, & Gaston, 2016), and there are 100 grains in the initial conditions for each simulation. Simplified physical parameters for grain boundary properties were chosen such that a reasonable amount of grain growth occurred in the time span of the weld pool simulation. Figure 13 shows the microstructures in both RVEs at the end of the simulation time (t = 2779 s). The average grain size in the RVE at y = 0.5 mm is larger than that in the RVE at y = 0.3 mm. The higher temperatures throughout the simulation for the RVE at y = 0.5 mm cause the grain boundary mobility to be greater there, resulting in faster grain growth.

Future work on the ALE method will include on-the-fly remeshing. This remeshing capability is necessary to prevent element inversion at the surface of the melt pool that can occur when accounting for the tangential forces of the Marangoni effect. We may also explore explicit modeling of the solid to liquid phase transition to capture the influence of the solidification process on the final part microstructure more completely.

1.1.5 Conclusions

The modeling and simulation development efforts discussed in this chapter represent important advances towards reliably predicting the performance of parts produced using AM techniques. Modeling and simulation approaches contribute significantly to the understanding of the physics governing the final part microstructure. The approaches in MOOSE and MALAMUTE discussed here represents the foundational efforts to develop PSPP correlations for two different AM techniques. The code development efforts in MOOSE and MALAMUTE have been used to investigate the role of non-uniform process parameter fields, including electric potential, temperature, and stress, on the microstructure evolution. Although these AM techniques represent innovative approaches to many challenges facing the manufacturing industry, an established connection between the manufacturing process parameters and the desired final microstructure is an area of active research. Through the multiphysics and multiscale capabilities of MOOSE and MALAMUTE, this connection can be explored and further developed.

As emerging and transformative technologies, AM techniques have shown significant benefits in the areas of aerospace, transportation, and construction, among many others. The benefits of AM techniques include reduced energy usage, better material efficiency, and increased part geometry complexity. Many AM methods make using advanced materials, particularly those difficult to manufacture with conventional methods, possible. Many advanced materials have demonstrated better performance in the extreme environments common in nuclear energy. Continued modeling and simulation efforts will advance the use of these materials and manufacturing techniques within the area of nuclear energy.

1.1.6 Acknowledgements

This work supported through the INL Laboratory Directed Research & Development (LDRD) Program under DOE Idaho Operations Office Contract DE-AC07-05ID14517. The mesoscale sintering work was performed in conjunction with the Interfacial Multiphysics Lab at Purdue University.

1.1.7 References

Anselmi-Tamburini, U., & Groza, J. R. (2017). Critical assessment 28: electrical field/current application--a revolution in materials processing/sintering? *Materials Science and Technology, 33*(16), 1855-1862.

Anselmi-Tamburini, U., Spinolo, G., Maglia, F., Tredici, I., Holland, T. B., & Mukherjee, A. K. (2012). Field Assisted Sintering Mechanisms. In *Sintering. Engineering Materials* (pp. 159-194). Berlin, Heidelberg: Springer.

Apostolakis, G., & Lemon, D. (2005). A Screening Methodology for the Identification and Ranking of Infrastructure Vulnerabilities due to Terrorism. *Risk Analysis, 25*(2), 361-376.

Asoro, M., Ferreira, P. J., & Kovar, D. (2014). In situ transmission electron microscopy and scanning transmission electron microscopy studies of sintering of Ag and Pt nanoparticles. *Acta Materialia, 81*, 173-183.

ASTM Committee F42 on Additive Manufacturing Technologies and ASTM Committee F42 on Additive Manufacturing Technologies. Subcommittee F42. 91 on Terminology. (2012). *Standard terminology for additive manufacturing technologies.* ASTM International.

Averú, A. C., Biehl, L. V., Medeiros, J. L., & Souza, J. D. (2016). Comparitive Study of the Diffusibility of a Nickel Alloy composed by Ni-Cr-Fe. *International Journal of Engineering Research & Technology, 5*(12).

Basu, P. C., Ravindra, M. K., & Mihara, Y. (2017). Component Fragility for Use in PSA of Nuclear Power Plant. *Nuclear Engineering and Design*, 209-227.

Biswas, S. (2017). *Multiphysics modeling for predicting microstructural evolution of powder materials during solid-state sintering.* Purdue University.

Biswas, S., Schwen, D., & Tomar, V. (2018). Implementation of a phase field model for simulating evolution of two powder particles representing microstructural changes during sintering. *Journal of Materials Science, 53*, 5799-5825.

Biswas, S., Schwen, D., Singh, J., & Tomar, V. (2016). A study of the evolution of microstructure and consolidation kinetics during sintering using a phase field modeling based approach. *Extreme Mechanics Letters, 7*, 78-89.

Biswas, S., Schwen, D., Wang, H., Okuniewski, M., & Tomar, V. (2018). Phase field modeling of sintering: Role of grain orientation and anisotropic properties. *Computational Materials Science, 148*, 307–319.

Box, G. T. (1992). *Bayesian Inference in Statistical Analysis.* John Wiley & Sons.

Brashear, J., & Jones, J. (2010). Risk Analysis and Management for Critical Asset Protection (RAMCAP Plus). In *Wiley Handbook of Science and Technology for Homeland Security.*

Brown, G., & Cox, L. (2011). How Probabilistic Risk Assessment Can Mislead Terrorism Risk Analysis. *Risk Analysis, 31*(2), 196-204.

Brown, G., & Cox, L. (2011). Making Terrorism Risk Analysis Less Harmful and More Useful: Another Try. *Risk Analysis, 31*(2), 193-195.

Butcher, J. C. (2008). *Numerical Methods for Ordinary Differential Equations.* Wiley.

Casagranda, A., & Sofronis, P. (1997). Numerical Observations of Scaling Laws in the Consolidation of Powder Compacts. *Acta Materialia, 45*(11), 4835-4845.

CASL. (n.d.). *The Consortium For Advanced Simulation Of Light Water Reactors*. Retrieved 2021, from https://casl.gov/

Cincotti, A., Locci, A. M., Orrù, R., & Cao, G. (2007). Modeling of SPS Apparatus: Temperature, Current and Strain Distribution with No Powders. *Materials, Interfaces, and Electrochemical Phenomena, 53*(3), 703-719.

Cipollaro, A., & Lomonaco, G. (2016). Contributing to the nuclear 3S's via a methodology aiming at enhancing the synergies between nuclear security and safety. *Progress in Nuclear Energy, 86*, 31-39.

Contini, S., Cojazzi, G., & Renda, G. (2008). On the use of non-coherent fault trees in safety and security studies. *Reliability Engineering & System Safety, 93*(12), 1886-1895.

Courtois, M. (2014). A complete model of keyhole and melt pool dynamics to analyze instabilities and collapse during laser welding . *Journal of Laser Applications, 26*(4).

Cox, L. (2008). Some Limitations of "Risk = Threat x Vulnerability x Consequence" for Risk Analysis of Terrorist Attacks. *Risk Analysis, 28*(6), 1749-1761.

Cox, L. (2009). Improving Risk-Based Decision Making for Terrorism Applications. *Risk Analysis, 29*(3), 336-341.

D. Gaston et al. (2009). MOOSE: A parallel computational framework for coupled systems of nonlinear equations. *Nucl. Eng. Des.,, 239*, 1768–1778. Retrieved from https://doi.org/10.1016/j.nucengdes.2009.05.021

Dana A. Knoll, D. E. (2004). Jacobian-free Newton-Krylov methods: a survey of approaches and applications. *Journal of Computational Physics, 193*(2), 357–397. doi:10.1016/j.jcp.2003.08.010

Dass, A., & Moridi, A. (2019). State of the art in directed energy deposition: from additive manufacturing to materials design. *Coatings, 9*(7), 418.

DOE/NEAMS. (n.d.). Retrieved 2021, from Nuclear Energy Advanced Modeling and Simulation Program: https://inl.gov/neams/

Durán, F., Wyss, G., Jordan, S., & Cipiti, B. (2014). Risk-Informed Management of Enterprise Security: Methodology and Applications for Nuclear Facilities. *International Conference on Nuclear Security: Enhancing Global Efforts.* Vienna.

Ezell, B., & Collins, A. (2011). Letter to the Editor. *Risk Analysis, 31*(2), 192.

Ezell, B., Bennett, S., Winterfeldt, D., Sokolowski, J., & Collins, A. (2010). Probabilistic Risk Analysis and Terrorism Risk. *Risk Analysis, 30*(4), 575-589.

Fahad Alsayyari, M. T. (2020). A nonintrusive adaptive reduced order modeling approach for a molten salt reactor system. *Annals of Nuclear Energy, 141*, 107321.

Fakhravar, D., Khakzad, N., Reniers, G., & Cozzani, V. (2017). Security Vulnerability Assessments of Gas Pipelines Using Discrete-Time Bayesian Network. *Process Safety and Environmental Protection, 111*, 714-725.

Gandhi, S., & Kang, J. (2013). Nuclear Safety and Nuclear Security Synergy. *Annals of Nuclear Energy, 60*, 357-361.

Garcia, M. (2006). *Vulnerability Assessment of Physical Protection Systems.* New York: Elsevier.

Garcia, M. (2008). Analysis and Evaluation. In *The Design and Evaluation of Physical Protection Systems: Second Edition* (pp. 261-299). New York: Elsevier.

Garcia, M. (2008). Design and Evaluation of Physical Protection Systems. In *The Design and Evaluation of Physical Protection Systems: Second Edition* (pp. 1-13). New York: Elsevier.

Gaston, D. R., Permann, C. J., Peterson, J. W., Slaughter, A. E., Andrs, D., Wang, Y., . . . Martineau, R. C. (2015). Physics-based multiscale coupling for full core nuclear reactor simulation. *Annals of Nuclear Energy, 84*, 45-54.

Geist, A. e. (1993). *PVM (Parallel Virtual Machine) User's Guide and Reference Manual.* Oak Ridge National Laboratory, ORNL/TM-12187.

Gibson, I., Rosen, D., & Stucker, B. (2015). *Additive Manufacturing Technologies.* New York.: Springer.

Giraud, J. G. (2019). Development of a cold plug valve with fluoride salt. *EPJ Nuclear Sciences & Technologies*.

Gottlieb, E., Harrigan, R., McDonald, M., Oppel, F., & Xavier, P. (2001). *The Umbra Simulation Framework.* Albuquerque: Sandia National Laboratories.

Greenquist, I., Tonks, M. R., Aagesen, L. K., & Zhang, Y. (2020). Development of a microstructural grand potential-based sintering model. *Computational Materials Science, 172*.

Hart, B., Hart, D., Gayle, R., Oppel, F., Xavier, P., & Whetzel, J. (2017). Dante Agent Architecture for Force-On-Force Wargame Simulation and Training. *The Thirteenth AAAI Conference on Artificial Intelligence and Interactive Digital Entertainment.* Snowbird. UT.

Huang, P.-H. (1995). Taiwan Power Company's Power Distribution. *Nuclear, 112*(2), 214-226. doi:10.13182/NT95-A35175

Hussein, A., Hao, L., Yan, C., & Everson, R. (2013). Finite element simulation of the temperature and stress fields in singlelayers built without-support in selective laser melting. *Materials and Design, 52*, 638-647.

Icenhour, C. T., Lindsay, A. D., Martineau, R. C., & Shannon, S. (2019). Electromagnetics Simulations with Vector-valued Finite Elements in MOOSE. *SIAM Conference on Computational Science and Engineering.* Spokane, WA, USA.

International Nuclear Safety Group. (2010). *The Interface Between Safety and Security at Nuclear Power Plants (INSAG-24).* Vienna: International Atomic Energy Agency.

Ishii, M. &. (2010). *Thermo-fluid dynamics of two-phase flow. .* Springer Sciences and Business Media.

Jiang, W., Spencer, B. W., & Dolbow, J. E. (2020). Ceramic nuclear fuel fracture modeling with the extended finite element method. *Engineering Fracture Mechanics, 223*(106713).

Kaplan, S., & Garrick, B. (1981). On the Quantitative Definition of Risk. *Risk Analysis, 1*(1).

Kareer, A., Waite, J. C., Li, B., Couet, A., Armstrong, D. E., & Wilkinson, A. J. (2019). Short communication: 'Low activation, refractory, high entropy alloys for nuclear applications'. *Journal of Nuclear Materials, 526*(151744).

Kelager, M. (2006, Jan 9). *Lagrangian Fluid Dynamics Using Smoothed Particle Hydrodynamics .* Retrieved Feb 20, 2021, from http://image.diku.dk/projects/media/kelager.06.pdf

Kelley, C. T. (1995). *Iterative Methods for Linear and Nonlinear Equations.* Society for Industrial and Applied Mathematics.

Kelly, D., & Curtis, S. (2011). *Bayesian Inference for Probabilistic Risk Assessment: A Practitioner's Guidebook.* Springer.

Khakzad, N., Reniers, G., & Gelder, P. (2017). A Multi-Criteria Decision Making Approach to Security Assessment of Hazardous Facilities. *Journal of Loss Prevention in the Process Industries, 48*, 234-243.

Kim, D., & Kang, J. (2012). Where Nuclear Safety and Security Meet. *Bulletin of the Atomic Scientists, 68*(1), 86-93.

Lawrence Livermore National Laboratory. (2018). *Joint Conflict and Tactical Simulation (JCATS) Capabilities Brief.* Livermore: Lawrence Livermore National Laboratory.

Le, T., Parks, J., & Noel, T. (2018). Mixed Reality 3D Tabletop Tool with Radioactive Source Model Visualization. *International Conference on the Security of Radioactive Material: The Way Forward for Prevention and Detection.* Vienna.

Li, L., Post, B., Kunc, V., Elliott, A. M., & Paranthaman, M. P. (2017). Additive manufacturing of near-net-shape bonded magnets: Prospects and challenges. *Scripta Materialia, 135*, 100-104.

Lindsay, A., Stogner, R., Gaston, D., Schwen, D., Matthews, C., Jiang, W., . . . Martineau, R. (2021). Automatic Differentiation in MetaPhysicL and Its Applications in MOOSE. *Nuclear Technology*.

Locci, A., Orrù, R., & Cao, G. (2020). Modeling of Electric Current Assisted Sintering: An extended fluid-like approach for the description of powders rehological behavior. *Chemical Engineering Reserach and Design, 154*, 283-302.

Lucoff, T. M. (1974). *TOPICAL REPORT POWER DISTRIBUTION CONTROL AND.* Pittsburgh, Pennsylvania: WESTINGHOUSE ELECTRIC CORPORATION.

Lunn, D., Jackson, C., Best, N., Thomas, A., & Spiegelhalter, D. (2013). OpenBUGS Documentation. In *The BUGS Book: A Practical Introduction to Bayesian Analysis.* CRC Press. Retrieved from openbugs.net: openbugs.net

Madison, J. D., & Aagesen, L. K. (2012). Quantitative Characterization of Porosity in Laser Welds of Stainless Steel. *Scripta Materialia, 67*(9), 783-786.

Mahadevan, J. R. (2009). Consistent and accurate schemes for coupled neutronics thermal-hydraulics reactor analysis. *Nuclear Engineering and Design, 239*, 566-579.

Manière, C., Lee, G., McKittrick, J., & Olevsky, E. A. (2018). Energy efficient spark plasma sintering: Breaking the threshold of large dimension tooling energy consumption. *Journal of the American Ceramic Society, 102*, 706-716.

Merle-Lucotte, E. H. (2013). Recommendations for a demonstrator of molten salt fast reactor. *IAEA-CN-199.* Paris, France.

Moelans, N., Blanpain, B., & Wollants, P. (2008). An introduction to phase-field modeling of microstructure evolution. *Calphad, 32*(2), 268-294.

Monaghan, J. J. (1992). Smoothed Particle Hydrodynamics. *Annual Review of Astronomy and Astrophysics, 30*, 534-574.

Moore, D., Fuller, B., Hazzan, M., & Jones, J. (2007). Development of a security vulnerability assessment process for the RAMCAP chemical sector. *Journal of Hazardous Materials, 142*(3), 689-694.

Neutrino Documentation. (n.d.). (GitHub) Retrieved Feb 20, 2021, from https://neutrinodocs.readthedocs.io/

Noble, D. R. (2007). *Use of Aria to Simulate Laser Weld Pool Dynamics for Neutron Generator Production.* Sandia National Laboratories.

NURESIM. (n.d.). *European Platform for Nuclear Reactor Simulations.* Retrieved 2021, from https://cordis.europa.eu/project/id/516560

NURESIP. (n.d.). *Nuclear Reactor Integrated Simulation Project.* Retrieved 2021, from https://cordis.europa.eu/project/id/232124

Olsson, E., & Kreiss, G. (2005). A conservative level set method for two phase flow. *Journal of Computational Physics, 210*(1), 225-246.

Osborn, D. (2017). Integrated Safety-Security Methodology for Loss of Large Area Analysis. Singapore: Sandia National Laboratories.

Parnell, G., Smith, C., & Moxley, F. (2010). Intelligent Adversary Risk Analysis: A Bioterrorism Risk Management model. *Risk Analysis, 30*(1), 32-48.

Permann, C. J., Gaston, D. R., Andrs, D., Carlsen, R. W., Kong, F., Lindsay, A. D., . . . Martineau, R. C. (2020). MOOSE: Enabling massively parallel multiphysics simulation. *SoftwareX, 11*(100430).

Permann, C. J., Tonks, M. R., Fromm, B., & Gaston, D. R. (2016). Order Parameter Remapping Algorithm for 3D Phase Field Model of Grain Growth Using FEM. *Computational Materials Science, 115*, 18-25.

Peter German, J. C. (2019). Application of multiphysics model order reduction to doppler/neutronic feedback. *EPJ Nuclear Sciences & Technologies, 5*.

Porter, D., & Easterling, K. (1992). *Phase Transformations in Metals and Alloys.* London: Chapman and Hall.

Price, J. F. (2006, June 7). *Lagrangian and Eulerian Representations of Fluid Flow:Kinematics and the Equations of Motion.* Retrieved Feb 20, 2021, from Woods Hole Oceanographic Institution: https://www.whoi.edu/science/PO/people/jprice/class/ELreps.pdf

Qin, Y., Wu, J., Hu, Q., Ghista, D. N., & Wong, K. K. (2017). Computational evaluation of smoothed particle hydrodynamics for implementing blood flow modelling through CT reconstructed arteries. *Journal of X-Ray Science and Technology*, 213-232.

Quarteroni, A., & Valli, A. (2008). *Numerical Approximation of Partial Differential Equations .* Springer .

RP., P. (2014). *New multiphysics coupling tools for trilinos:.* Sandia National Lab. Technical Report.

Ryan, E. D. (2019). *Determination, Development, and Validation of a Fluid Height Analysis Method and Particle Spacing Protocol for the Smoothed Particle Hydrodynamic Code Neutrino .* Pocatello: Idaho State University.

Ryan, E. D., & Pope, C. L. (2019). Coupling of the Smoothed Particle Hydrodynamic Code Neutrino and the Risk Analysis Virtual Environment for Particle Spacing Optimization. *Nuclear Technology* , 1506-1516.

Ryan, E. D., Savage, B. M., Smith, C. L., & Pope, C. L. (2019). Comparison of free surface flow measurements and smoothed particle hydrodynamic simulation for potential nuclear power plant flooding simulation. *Annals of Nuclear Energy, 126*, 389-397.

Saad, Y. (2003). *Iterative Methods for Sparse Linear Systems.* Society for Industrial and Applied MAthematics.

Smith, J., Xiong, W., Yan, W., Lin, S., Cheng, P., Kafka, O. L., . . . Liu, W. (2016). Linking process, structure, property, and performance for metal-based additive manufacturing: computational approaches with experimental support. *Computational Mechanics, 57*, 583-610.

Sridharan, N., Gussev, M. N., & Field, K. G. (2019). Performance of a ferritic/martensitic steel for nuclear reactor applications fabricated using additive manufacturing. *Journal of Nuclear Materials, 521*, 45-55.

Stein, M., & Morichi, M. (2012). Safety, Security, and Safeguards by Design: An Industrial Approach. *Nuclear Technology, 179*(1), 150-155.

Steinbach, I. (2009). Phase-field models in materials science. *Modelling and Simulation in Materials Science and Engineering, 17*(7), 073001.

Stender, M. E., Beghinia, L. L., Sugar, J. D., Veilleux, M. G., Subia, S. R., Smith, T. R., . . . Dagel, D. J. (2018). A thermal-mechanical finite element workflow for directed energy deposition additive manufacturing process modeling. *Additive Manufacturing, 21*, 556-566.

Steven Hamilton, M. B. (2016). An assessment of coupling algorithms for nuclear reactor core physics simulations. *Journal of Computational Physics, 311*, 241–257.

Strickland, E. (2011, October 31). 24 Hours at Fukushima. *IEEE Spectrum*.

Sun, C., Wang, Y., McMurtrey, M. D., Jerred, N. D., Liou, F., & Li, J. (2021). Additive manufacturing for energy: A review. *Applied Energy, 282*, 116041.

Tano, M. (2018). *Development of multi-physical multiscale models for molten salts at high temperature and their experimental validation.* PhD Dissertation, Université Grenoble Alpes.

Tano, M. R. (2018). Multiphysics study of the draining transients in the Molten Salt Fast Reactor. *International Congress on Advances in Nuclear Power Plants (ICAPP 2018).*

Tautges TJ, M. R. (2004). *MOAB: a Mesh-Oriented.* Sandia National Laboratories, SAND2004-1592.

Udell, C., Tilden, J., & Toyooka, R. (1993). Modified Risk Evaluation Method. *Institute of Nuclear Materials Management 34th Annual Meeting.* Scottsdale.

United States Department of Energy, Office of Energy Efficiency and Renewable Energy. (2019). Advanced Manufacturing Office Fact Sheet. Washington D.C.

United States Nuclear Regulatory Commission. (2020, March 31). *Frequently Asked Questions About Force-on-Force Security Inspections at Nuclear Power Plants.* Retrieved October 05, 2020, from https://www.nrc.gov/security/faq-force-on-force.html

United States Nuclear Regulatory Commission. Title 10, Code of Federal Regulations, Part 73 Section 55. (n.d.). *Requirements for Physical Protection of Licensed Activities in Nuclear Power Reactors Against Radiological Sabotage*. Retrieved from https://www.nrc.gov/reading/rm/doc-collections/cfr/part073/part073-0055.html

Unity Technologies. (n.d.). Retrieved October 13, 2020, from www.unity.com

Varnado, G., & Whitehead, D. (2008). *Vital Area Identification for U.S. Nuclear Regulatory Commission Nuclear Power Reactor Licensees and New Reactor Applicants SAND2008-5644.* Albuquerque: Sandia National Laboratories.

VERA. (n.d.). Retrieved 2021, from The Virtual Environment for Reactor Applications: https://vera.ornl.gov/

Verma, D., Biswas, S., Prakash, C., & Tomar, V. (2017). Relating Interface Evolution to Interface Mechanics Based on Interface Properties. *JOM, 69*(1), 30-38.

Vijay S Mahadevan, J. C. (2012). A verification exercise in multiphysics simulations for coupled reactor physics calculations. *Progress in Nuclear energy, 55*, 12-32.

Vijay, M., E., M., T., T., & al., e. (2013). High-resolution coupled physics solvers for analysing fine-scale nuclear reactor design problems. *Phil. Trans. R. Soc. A, 372*. Retrieved from http://dx.doi.org/10.1098/rsta.2013.0381

Weaver, W. L. (2005). *Programmers Manual For The PVM Coupling Interface In The RELAP5-3D Code.* Idaho National Laboratory, INL/EXT-05-00203.

Wells, A. (2020). *Nuclear Power Plant Component Fragility in Flooding Events Using Bayesian Regression Modeling with Explanatory Variables.* Pocatello: Idaho State University, Dissertation.

Wells, A., Ryan, E. D., Savage, B., Tahhan, A., Suresh, S., Muchmore, C., . . . Pope, C. L. (2019). Non-watertight door performance experiments and analysis under flooding scenarios. *Results in Engineering*.

Wen, S., & C.Shin, Y. (2010). Modeling of transport phenomena during the coaxial laser direct deposition process. *Journal of Applied Physics, 108*(4).

Why France is developing digital twins for the country's nuclear reactors. (2020, Dec.). Retrieved 2021, from https://www.nsenergybusiness.com/news/nuclear-reactors-digital-twins/

Williams, J. (1978). DOE/SS Handbooks-A Means of Disseminating Physical Security Equipment Information. *Journal of the Institute of Nuclear Materials Management, 7*(1), 65-76.

Xia, S., Gao, M. C., Yang, T., Liaw, P. K., & Zhang, Y. (2016). Phase stability and microstructures of high entropy alloys ion irradiated to high doses. *Journal of Nuclear Materials, 480*, 100-108.

Xie, Z., Jiang, W., Congjian, W., & Xu, W. (2021). Bayesian Inverse Uncertainty Quantification of a MOOSE-based Melt Pool Model for Additive Manufacturing Using Experimental Data. *arXiv, arXiv:2105.05370v2*.

Zakariya, N., & Kahn, M. (2015). Safety, Security and Safeguard. *Annals of Nuclear Energy, 75*, 292-302.

Zhong, Y., Rannar, L.-E., Liu, L., Koptyung, A., Wikman, S., Olsen, J., . . . Shen, Z. (2017). Additive manufacturing of 316L stainless steel by electron beam melting for nuclear fusion applications. *Journal of Nuclear Materials, 486*, 234-245.